

Methodology for the characterisation of characteristic spectral profiles, applied to chromium $K\beta$

L. F. Smale,^a C. T. Chantler^{a*} and J. A. Kimpton^b

The investigation of tests of quantum electrodynamics in the X-ray regime down to 2–20 parts per million (ppm) amplifies the need for improved characterisation of asymmetric reference sources and energies in this regime. While several transition metal characteristic energies have been defined, most are not referenced to accurate profiles or robust links to the metre via X-ray optical interferometry. Lower intensity $K\beta$ transitions have relatively poor accuracy – we ask how to determine $K\beta$ transitions to an accuracy approaching those of $K\alpha$ transitions. Instrumental broadening normally encountered in X-ray experiments shifts the features of profiles used for calibration, such as peak energy, by a significant amount many times the quoted accuracies. We present a study of a methodology used recently to determine energies and profiles experimentally down to 4.5 and 2.7 ppm for Ti and V $K\beta$. In this study, we investigate the robustness of the methodology for a difficult data set and demonstrate that the approaches to and characterisation of the chromium $K\beta$ spectral profile are consistent with accurate measurements in the literature down to 24 ppm. The peak energy of the chromium $K\beta$ spectral profile is found to be 5946.68(14) eV prior to instrumental broadening. Characterisation of the spectral profile of the radiation, including the instrumental broadening, allows us to obtain an accurate and notably transferable standard. Significantly, we present a widely applicable methodology for achieving and using this standard. This approach has been used down to an accuracy of 2–5 ppm. Copyright © 2015 John Wiley & Sons, Ltd.

Introduction

High accuracy, absolute energy calibration is crucial to progress in X-ray science. Characteristic radiation – $K\alpha$ and $K\beta$ – produced with electron bombardment, where the incident electron energy is at least 2.5–3 times the threshold energy, is often used as a calibration standard as the profiles are stable and cheap to produce. These spectral profiles are robust under different excitation conditions, as they reflect the atomic and electronic structure of the elements. Characterisations of the profiles permit new tests and understanding of inner-shell processes and fundamental atomic theory, including quantum electrodynamics.^[1,2]

The structure is properly modelled through the relativistic quantum theory of the atom, which has seen recent improvement.^[3] A concerted effort to experimentally summarise experimental energies of characteristic radiation was undertaken and compiled by Bearden *et al.* in 1967.^[4] This has been complemented by theoretical computations by Desclaux^[5] and further experimental and theoretical compilation by Deslattes *et al.*^[6] That review work reports the energy of the dominant transition (diagram lines) without regard for the shifts and change of shape of the spectra due to satellite lines or profile asymmetry. It remains particularly difficult to compare advances in theory to high accuracy experiment. Significant advance in theory since then has been based on the relativistic approach of Grant.^[7]

Experimental spectral profiles for the characteristic radiation of transition metals are represented by semi-empirical fitting of multiple components – using typically five or seven peaks for $K\alpha$ spectra.^[8,9] Recent work has demonstrated that new approaches can yield a more robust standard.^[10–12] Conversely, theoretical modelling of characteristic radiation profile shape is dominated by diagram lines, representing X-ray emission energies detailing

the electron decay from atomic transitions: an excited electron with a core hole decays to the ground state with the core filled and a higher n hole. Additional components, theoretically and empirically, are contributed by satellite lines caused by shake-up and shake-off effects. This set of transitions is complex, especially for elements with open sub-shells such as the transition metals. Progress in the details of such theory has been slow until recently.^[13–16] Empirical modelling using fitting functions for a sum of a small number of Lorentzian, Gaussian, Voigt or instrumental functions fails to reveal the theoretical complexity of the many configuration state function transitions.

Efforts to find good empirical models of spectral radiation have continued from the work of Deutsch *et al.* and Hölzer *et al.* in the 1990s.^[8,9,17–19] Deslattes *et al.*^[6] include a summary of these efforts, summarised in Table 1 with experimental energies and uncertainties for $K\alpha$ characteristic peaks for Z from 22 to 26 and including Chantler *et al.*^[20] The uncertainties for the $K\alpha$ data are on the order of 1 to 2 parts per million (ppm). The uncertainty of the literature value of the chromium $K\beta$ peak energy^[4] (Table 1) is 1.7 ppm.

Data collection methods often use a single flat crystal spectrometer employing the Bond method^[8,9] or a curved crystal spectrometer.^[17] In the experimental work arising from

* Correspondence to: C. T. Chantler, School of Physics, University of Melbourne, Parkville, Melbourne 3010, Australia. E-mail: chantler@unimelb.edu.au

^a School of Physics, University of Melbourne, Parkville, Melbourne 3010, Australia

^b Australian Synchrotron, 800 Blackburn Road, Clayton, Melbourne 3168, Australia

Table 1. Characteristic radiation peak energy data from the literature

Spectral profile peak	Reference peak energy (eV)	Peak energy uncertainty (ppm)
Titanium $K\alpha_2$	4504.920	2.09
Titanium $K\alpha_1$	4510.899	2.08
Vanadium $K\alpha_2$	4944.651	2.22
Vanadium $K\alpha_1$	4952.131	1.21
Chromium $K\alpha_2$	5405.538	1.31
Chromium $K\alpha_1$	5414.804	1.31
Manganese $K\alpha_2$	5887.685	1.43
Manganese $K\alpha_1$	5898.801	1.42
Iron $K\alpha_2$	6391.03	1.5
Iron $K\alpha_1$	6404.01	1.5
Chromium $K\beta_1$	5946.82	1.7

The V $K\alpha$ data are from Chantler *et al.*^[20] the Fe $K\alpha$ and Cr $K\beta$ data are from Hölzer *et al.*^[9] and the rest of the data are from Deslattes *et al.*^[6]

Germany,^[8] raw spectra were deconvolved with a measured, fitted or simulated instrumental broadening, and each deconvolved spectrum was fit empirically. The peak location of each empirical fit was taken to be the measure of each peak energy. The deconvolution of spectra limits the understanding of error propagation. It is not immediately clear how to use these characterisations as standards for experiments with different instrumental broadening. Chantler *et al.*^[20] addressed this concern by providing a consistent set of empirical fit functions for a range of elements ($21 \leq Z \leq 25$) including an approach to allow for instrumental broadening effects.

There has been some interest in the shape of the Cr $K\beta$ profile recently.^[21–25] This work has related to the problematic peak reported by Bearden *et al.*^[4] Hölzer *et al.*^[9] reported an experimental line shape and peak energy (listed in Table 1). A theoretical calculation of the peak energy for the diagram line of Cr $K\beta$ is 5947.1(10) eV^[6] in good agreement with older theory and the experimental value but a much larger uncertainty than the experimental result. Given the recent characterisations of Ti $K\beta$ and V $K\beta$,^[10,11] it is valuable to investigate the robustness of this approach in comparison with alternate approaches. This is the subject of this paper.

This paper presents a measurement of chromium $K\beta$ and a characterisation of the profile as well as presenting a study of the robustness of the self-consistent determination of the dispersion function. The inclusion of broadening effects in the fitting method enables the results to be transferable to a larger range of experimental conditions. Specifically, the characterisation, or indeed the profile itself, can be simply used in experiments, where the amount of instrumental broadening is difficult to measure. More important than the energy determination, the profile definition, or the characterisation, is the demonstration of the methodology down to 24 ppm. We present a study of a methodology used recently to determine energies and profiles experimentally down to 4.5 and 2.7 ppm.^[10,11] We study chromium $K\beta$ as representative of the weaker $K\beta$ transitions, but with excellent previous measurement from the literature.^[6] Further, this data set is optimised for Ti $K\beta$ and V $K\beta$ as demonstrated by recent publications, but we here apply the methodology to the extreme edge of the calibration

region. We demonstrate that the approaches to and characterisation of the chromium $K\beta$ spectral profile are consistent with accurate measurements in the literature down to 24 ppm.

Method of investigation of the chromium $K\beta$ standard

To create a chromium $K\beta$ standard, the profile was measured using a wavelength dispersive technique, calibrated by the set of $K\alpha$ lines in Table 1. The calibration was optimised in a number of different ways to check the robustness and methodology. The $K\beta$ profile was fit with a sum of Voigt functions with a common Gaussian width to model instrumental broadening.

Experimental setup

The source of the $K\alpha$ radiation used for calibration and the measured Cr $K\beta$ line consisted of an electron gun firing 20 keV electrons at a collection of metal targets ($Z = 22–26$), each of which was placed in the electron beam separately. Data collection employed a Johann geometry curved crystal spectrometer with position-sensitive X-ray detection at the Oxford EBIT.^[26] Figure 1 shows the arrangement of the X-ray source, diffracting crystal and detector. The electron beam incident on the transition metal target results in the emission of characteristic X-ray radiation. The detector arm is set at a Bragg angle of 2θ , and an adjustable 'Seemann wedge' limits the diffracting region of illumination of the Germanium (220) Bragg crystal. The arm angle is fully adjustable, with low hysteresis on the gearing and high reproducibility. The housing for the crystal is mechanically linked to the detector arm, such that the normal vector to the crystal surface bisects the angle between the source and detector arm. Thus, the crystal angle (θ) is half the detector arm angle. The crystal and detector arm angles are measured by gravity-referenced electronic clinometers, each outputting a raw voltage, V . The V s are calibrated to θ . The Seemann wedge permits adjustment of the band-pass of radiation through the crystal and limits the instrumental broadening.

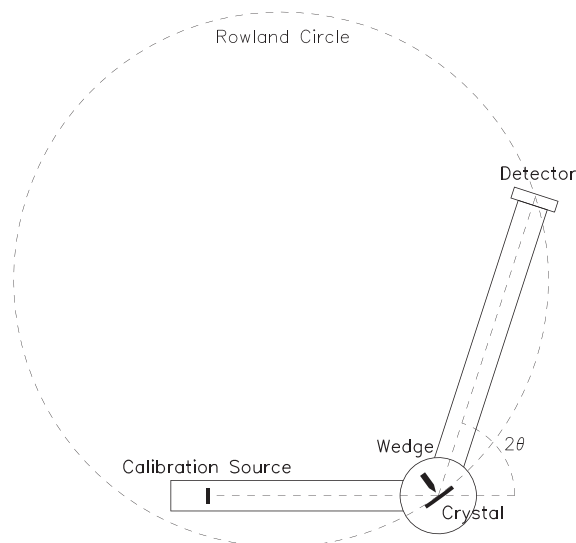


Figure 1. Schematic diagram of experimental setup. The calibration source is the source of the $K\alpha$ radiation used in calibration and the Cr $K\beta$ radiation. Details of the setup can be found in the Section on Experimental Setup.

By varying the wedge position, the crystal curvature perfection and the consistency of prediction from dynamical diffraction theory are investigated. A multi-wire gas-proportional counter with a backgammon configuration was used to detect the characteristic X-rays, providing good linearity and resolution in the dispersion (detector) axis and enabling the collection of position data for each X-ray detection event.

The electron gun was normal to both the path of the X-rays from the target to the crystal and to the path of the X-rays from the crystal to the detector. Transition metal targets were mounted at 45° to both the electron beam and the path from the selected target to the crystal. The radius of the spot size of the electron beam on the selected target was 5(1) mm. The distance from the target to the crystal was 350(3) mm, and the radius of the Roland circle was 1371(10) mm. The distance from the crystal to the active region of the detector was 1500(5) mm. The calibration source was placed in an off-focus position, to increase the accuracy and to reduce the sensitivity of the resulting spectra to the spacial intensity distribution of the source. The aim is to image the wavelength intensity distribution of the source, not its spacial intensity distribution.

The crystals of germanium were manufactured and calibrated by the National Institute of Standards and Technology (prior to curvature) and are near-perfect single crystals. There is, therefore, no mosaic spread and no orientational distribution function to include. Mosplate does indeed include any scale of mosaicity in the code and computation, so this would be easy to include; however, the crystals have none. Thermal (Debye-Waller) parameters are important and are included for the estimated temperature on an isotropic basis, as is normal for symmetric and monatomic solids. The value of σ^2 used is $0.5661(26)\text{\AA}^2$ for $T = 293\text{K}$, with a linear expansion coefficient of $5.7 \times 10^{-6}\text{K}^{-1}$.^[27]

For the calibration of the spectrometer, crystal alignment and detector scale, a series of calibration spectra was collected in successive diffracting positions in order to assess systematics and evaluate the dispersion function. Table 1 provides the list of reference lines with their energies and provenance, together with the Cr K β reference for comparison.

Diffraction theory

The experimental setup was modelled by the dynamical diffraction code, Mosplate.^[28,29] Mosplate predicts and models diffraction phenomena that have an effect on energy determination up to the order of 100 ppm and characterises these to an accuracy better than 1 ppm. These diffraction phenomena include lateral shifts in position due to X-rays penetrating the crystal to some depth and refractive index corrections. The refractive index shift, of order 100 ppm, must be determined accurately to 1% or better. Lateral shifts in curved crystal spectrometry may be of a similar order of magnitude. Corrections for asymmetry and polarisation are typically responsible for another 30 ppm, while depth penetration of the dynamical wavefield can dominate in curved crystal spectrometry but can be even more significant for flat crystal spectrometry.

For a particular X-ray energy, E , and crystal angle, θ , Mosplate calculates the X-ray intensity spectrum we expect to see on the detector. The incident wavefield is computed by ray tracing performed from a point grid at the source to a point grid on the cylindrically curved crystal. The wavefield is then propagated through the crystal to find the diffracted wavefield at the exit surface of the crystal. The diffracted field distributions in position and angle

at the crystal surface are then used as a source to ray trace to the detector. For each single energy, a range of spectra are calculated at different crystal angles. A peak position, D , is then computed for each of these spectra. These calculations are performed by sampling the Mosplate model function for the peak position, D , and profile as a function of peak energy, E , and crystal angle, θ :

$$D = D_{\text{mos}}(E, \theta) \quad (1)$$

This model also implicitly defines functions that calculate E and θ from the remaining variables:

$$E = E_{\text{mos}}(D, \theta) \quad (2)$$

$$\theta = \theta_{\text{mos}}(D, E) \quad (3)$$

For active use, these functions are interpolated between the sampling frequency of E and θ , for which the $D_{\text{mos}}(E, \theta)$ are computed to high accuracy. Interpolation uncertainty is negligible - well below 1 ppm.

Data collection

Seven calibration series were collected, each with a different wedge position and different integration times, so that the diffraction theoretical modelling must make accurate independent predictions of each geometry at each position. Within each calibration series, K α and K β spectral profiles from $Z = 22$ – 26 were collected. Each spectral profile type was collected at three to five arm angles, thereby sampling profiles and angular settings at different positions on the detector. This allowed detailed and independent investigations of the dispersion function and the detector response function. The remarkable consistency of the results demonstrates the robustness of the code and calibration methodology as discussed later; the remaining variance is thus an explicit characterisation of any systematic deficiencies, which could contribute to theoretical or experimental inconsistency or error.

K α profile modelling

For $Z = 22$ – 25 , K α profiles were fitted as functions of energy as defined by Chantler *et al.*^[20] Each of these functions is a sum of six Voigt profiles with a common Gaussian width to model the instrumental broadening, and maps X-ray energy to X-ray intensity. The energy offsets, Lorentzian widths and relative amplitudes of the Voigt profiles are defined by Chantler *et al.*^[20] For the $Z = 26$ Fe K α profile, the same type of data for a sum of Voigt profiles were given by Hölzer *et al.*^[9] Each of the K α experimental profiles were measured on a detector position axis rather than directly on an energy axis, so the profiles were fit by refining five fitting parameters:

1. a detector scale and
2. a detector offset to map the detector position to energy,
3. an intensity scale to model the overall intensity of the profile,
4. a constant intensity background, and
5. a common Gaussian broadening width.

These highly accurate K α characterisations allow the assignment of peak energies to the detector positions of each profile at each clinometer voltage. Figure 2 shows how one such fit leads to two calibration points for a measured Mn K α spectrum.

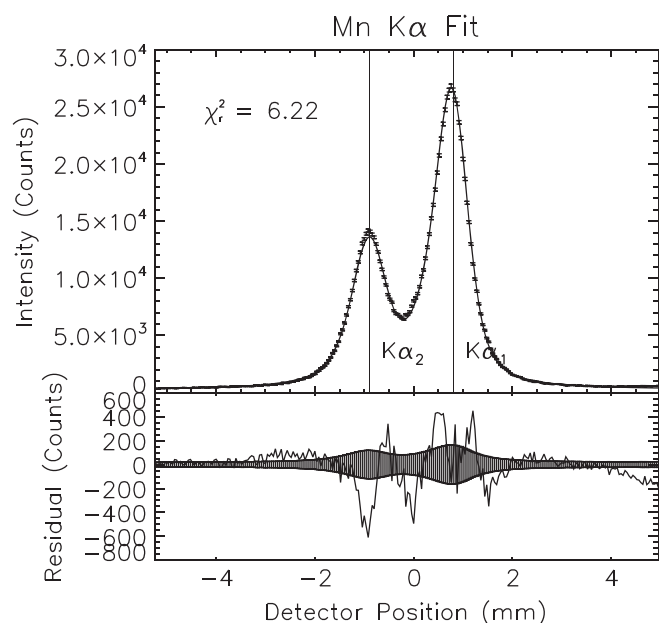


Figure 2. Typical fit of Mn Kα spectrum, yielding two calibration points (Mn Kα₁ and Mn Kα₂), which constrain the spectrometer dispersion function. This particular fit has a χ^2_r of 6.2. The Kα₁ peak has an energy of 5898.8010(84) eV and detector position of 0.8154(16) mm. The Kα₂ peak has an energy of 5887.6859(84) eV and detector position of -0.8850(25) mm. The crystal clinometer voltage was -2.2499502(79) V.

Chromium Kβ profile fitting

Twenty-seven Cr Kβ profiles were also collected and characterised on intensity and detector position axes. To define a characteristic line shape function, each of the spectra were fitted using a sum of four Voigt functions with a common Gaussian width, σ , and a constant intensity background, B . The i th Voigt function used in the characterisation is defined to be:

$$V(x; A_i, C_i, W_i, \sigma_i) = A_i \int_{-\infty}^{\infty} \frac{e^{-x'^2/(2\sigma_i^2)}}{\sigma_i \sqrt{2\pi}} \frac{W_i/2}{\pi[(x - C_i - x')^2 + (W_i/2)^2]} dx' \quad (4)$$

where A_i is the integrated area of the Lorentzian profile, C_i is the centroid of the profile, W_i is the Lorentzian full width at half maximum (FWHM) and σ_i is the Gaussian broadening stan-

dard deviation. The Gaussian broadening FWHM is $2\sqrt{2 \ln 2} \sigma_i \approx 2.35\sigma_i$. Thus, the spectra containing a Cr Kβ spectral profile were modelled with

$$P(x; B, \sigma, A_1, C_1, W_1, A_2, C_2, W_2, A_3, C_3, W_3) = B + \sum_{i=1}^3 V(x; A_i, C_i, W_i, \sigma_i = \sigma) \quad (5)$$

All 27 measured Cr Kβ profiles were separately fitted with this method. The relative intensities, positions and width parameters of the Voigt functions were consistent with one another, so the minimum uncertainty functionals are reported. The fits were done with a sum of four Voigt functions, though one of the Voigt function intensities hit the fitting constraint that enforced a non-negative Voigt function intensity. This means that three Voigt functions were sufficient to represent Cr Kβ as measured. The characteristic parameters of these fits are shown in Table 2 with the position axis converted to energy. Figure 3 shows a typical fit for one of the Cr Kβ spectra.

These characteristic parameters were then used to constrain refits of all the Cr Kβ profiles. Each refit had free parameters characterising the overall intensity, position, detector position to energy scale conversion, instrumental broadening and background of the spectral profile in the specific geometry of the measurement. As each refit had a slightly different instrumental broadening due to geometry changes, the transferable reference position of each profile peak was taken to be the position of the maximum of the fit function with the Gaussian width set to zero. All refits were reliable and consistent with the original fits: the characterisation allows for a consistent transferable standard in this measurement, in the calibration of the dispersion function, and for any subsequent independent measurement by other authors. This enables a consistent measurement of peak position of Cr Kβ spectra for any particular instrumental broadening, where the spectra are not significantly vignetted by the effects of source size or a slit width. Fitting spectra with this method would reveal the significance of any such vignetting by returning a high χ^2_r value for the fits. In the current situation, the method enabled a more consistent use of the literature experimental and theoretical standards.

Optimisation of the dispersion function

The Appendix describes the mathematical formalism for summarising the fitting procedure for the dispersion function used for the data analysis and the core methodology for deriving a series

Table 2. Characterisation of the Cr Kβ spectral profile

Relative area $\frac{A_i}{\sum_{i=1}^3 A_i}$	Integrated area A_i (counts)	Centroid C_i (eV)	FWHM W_i (eV)
0.333(20)	219011(13177)	5937.00(31)	19.84(60)
0.209(18)	137415(11971)	5943.70(16)	5.74(32)
0.458(15)	300778(9767)	5946.705(24)	2.37(11)

The profile is characterised on an absolute energy scale using a sum of component Lorentzians convolved with a common Gaussian instrumental broadening. Integrated areas (A_i), centroids (C_i) and FWHMs (W_i) of individual components were obtained from a series of fits of intensity against detector position. The detector position axis was then transformed to an absolute energy scale using the calibration procedure. The Gaussian width $\sigma = 1.517(32)$ eV. The background was $B = 629(23)$ counts. The third component dominates the height of the profile, while the first and second components fill out the low energy profile asymmetry.

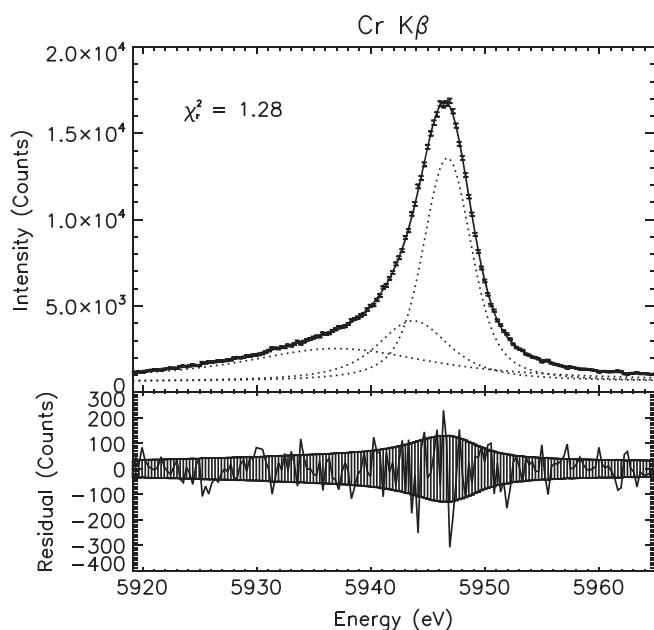


Figure 3. Typical fit of a Cr K β spectrum. The points with error bars are the experimental data, the solid line is the fitted sum of Voigt functions, and the three dotted lines are the three individual Voigt components with the background offset. The corresponding fitting parameters are provided in Table 2.

of fitted energy determinations of chromium K β from the dispersion function. The fitting procedure used in this work is improved from that of previous results^[10,11] by: (1) the inclusion of the Fe K α_1 and Fe K α_2 data in the calibration fitting; and (2) the pooling of all K α data for a given wedge position into the same fit rather than separating them by wedge and collection time. The uncertainties near Cr K β are large due to it being on the edge of the range of arm angles included in the fitting procedure so that the addition of the Fe K α data better constrained the dispersion fits in the Cr K β arm angle range. The pooling of calibration data by wedge position led to a better distribution of good data and therefore less variance in the Cr K β peak energy.

A key question on robustness is whether the optimisation criteria can distort the analysis, variance and result. If robust and consistent, the optimised result should minimise variance and preserve a consistent central energy determination. Hence, we investigated the self-consistency of a series of alternate optimisations, each minimising a different measure of quality of the calibration fitting. These are measures (a) through (e). Each optimisation was a three-step process:

1. for a range of detector scales, there was a fit of I_{data} versus V (defined in the Appendix), which refined the clinometer calibration function in the context of that detector scale;
2. for each detector scale, a calculation of the measure to be minimised was made; and
3. the detector scale and clinometer calibration function that minimised the measure was then selected.

The first and third optimisations have been used in past analyses to determine the energy and profile of Ti K β and V K β . Following these past results, the range of energy of interest in this study is and should be that of Cr K β . We provide the others to prove both that they are consistent and to reveal difficulties of the minimisa-

tion. Figure 4(a)–(e) provides the resulting distributions of Cr K β peak energies for each of the optimisations.

The first optimisation (Fig. 4(a)) minimised measure (a): the χ_r^2 value of the Ti K β peak energy measurements (preferred in the work of Chantler *et al.*^[11]). In this optimisation of the set of independent measurements of the Cr K β peak energy, there is a clear slope in the results for each calibration series that represents a possible systematic error in $P_{D,1}$, the detector scale parameter. This is a result of $P_{D,1}$ being optimised only for crystal angles where the Ti K β line was measured. The remainder of optimisations (Fig. 4(b)–(e)) was minimising combinations of the dispersion of Ti K β , V K β , Cr K β and the K α lines.

The second optimisation (Fig. 4(b)) minimised measure (b): the sum of two values – (1) the χ_r^2 value of the Ti K β peak energy measurements, and (2) the χ_r^2 value of the V K β peak energy measurements.

The third optimisation (Fig. 4(c)) minimised measure (c): the χ_r^2 value of the V K β peak energy measurements (preferred in the work of Smale *et al.*^[10]).

The fourth optimisation (Fig. 4(b)) minimised measure (d): the sum of four values – (1) the χ_r^2 value of the Ti K β peak energy measurements, (2) the χ_r^2 value of the V K β peak energy measurements, (3) the χ_r^2 value of the Cr K β peak energy measurements, and (4) the χ_r^2 value of the clinometer calibration function fit which is a measure of the spread of the K α data around the literature values.

The last optimisation (Fig. 4(e)) minimised measure (e): the χ_r^2 value of the Cr K β peak energy measurements. It is to be expected that the uncertainty in the region of interest is minimised by this approach, and that the result is likely to be optimum using this last method. By definition, the systematic error reflected in the slope of each calibration is minimised. Note that this optimisation only locally minimises this systematic around the Cr K β arm angles, away from this range, the systematic is visible.

What insight is presented in the comparisons of these figures? They demonstrate that all wedge settings are not uniformly well defined, and that while the uncertainty of each point from the statistical fitting is very well defined, of order 2–3 ppm, the systematic uncertainties clearly dominate and are some 10 times this value. Earlier analysis and past results for Ti K β and V K β ^[10,11] used data from Sc K α through Mn K α but neglected Fe K α . The divergence of constraint at Cr K β energies demanded the inclusion of analysis of Fe K α profiles so that the dispersion function was interpolated rather than extrapolated to the region of interest. Nonetheless, the constraint was not uniformly effective because the quantity and quality of the individual peak profiles varied from one wedge setting to another. Hence, the collection of profiles for each wedge setting will not in general be equally well defined. Perhaps more importantly, this study demonstrates that any sensible optimisation system yields a similar agreement and pattern of discrepancy, and a similar final uncertainty. We investigated a more extensive set, but these illustrate the general principle that under normal circumstances this methodology is robust.

The remaining error (scatter) between the calibration runs reflects that Cr K β was at the far edge of the calibrated region of the crystal angle range, so that the variance observed is deliberately maximised in this study. We emphasise that effectively the same dispersion function and optimisation as presented in measure (a) yielded no large systematic in the energy regime of Ti K β and yielded a final consistency at the $\sigma = 4.5$ ppm level or

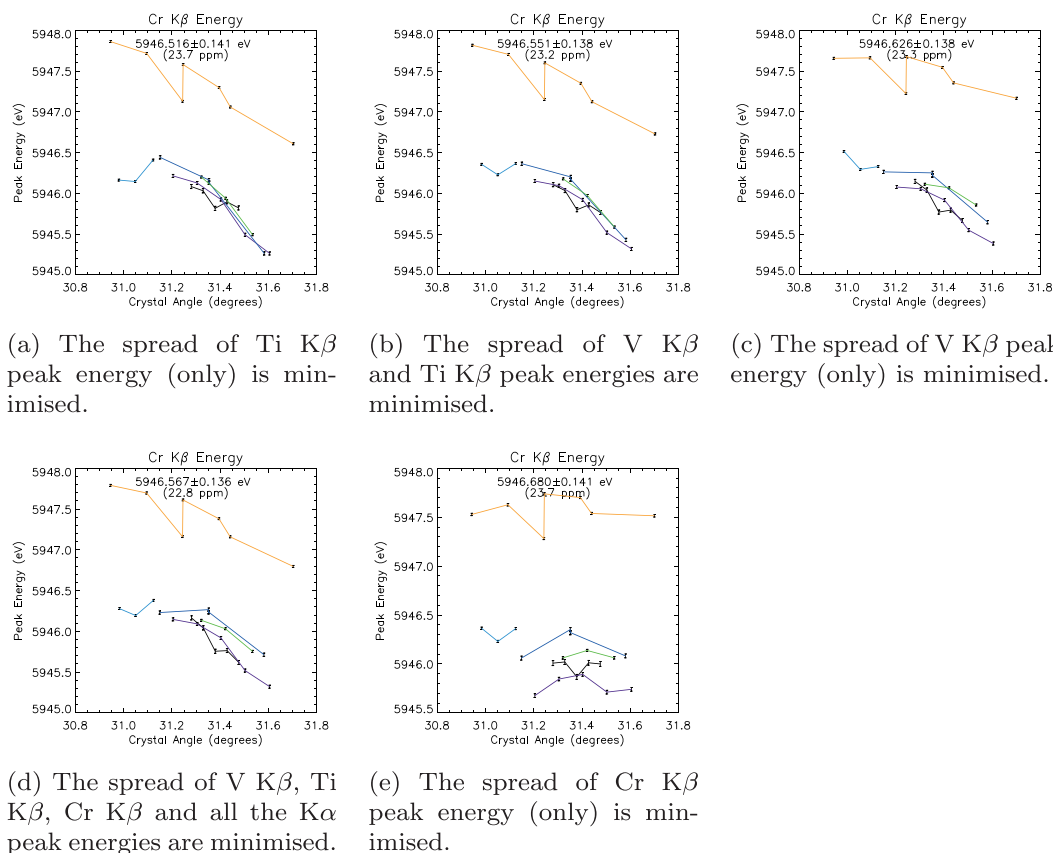


Figure 4. The Cr K β peak energies of individual measured spectra. Each sub-figure is the result of a different χ_r^2 measure that has been optimised – measures (a)–(e). Each of the six lines in each sub-figure are results from a single wedge position, derived by methodical stepping the spectrometer arm angle so that the profile is stepped across the detector area. Each point fit is statistically precise to 1–3 parts per million, but the scatter between wedges and positions is less accurate. The slopes from left to right in Fig. 4(a)–(d) are indicative of a correlation between the dispersion function (energy versus diffracting angle) and the detector calibration (energy or angle versus detector position). This systematic results from the correlation of parameters and the fact that this has not been minimised in these plots. Measure (e) (Fig. 4(e)) reduces this systematic in the energy region of Cr K β and is sufficient to yield an accurate determination of the detector scale and minimisation of slope systematics, with a smaller variance and dispersion. While it also yields a higher accuracy, it remains consistent with the earlier optimisations and methods.

± 0.022 eV,^[11] while that presented in measure (c) yielded no large systematic in the energy regime of V K β and yielded a final consistency at the $\sigma = 2.7$ ppm level or ± 0.015 eV.^[11] Indeed, in the latter measurement and characterisation, the individual point uncertainties were 1.6 ppm. The point is that we expect and observe divergences due to limited accuracy of subsets with different wedge settings near the edge of the interpolation region.

Figure 5 presents the weighted mean values of the peak energy for each optimisation (measures (a)–(e)) in comparison to the peak energy reported by Hölzer *et al.*^[9] The energies reported here are all consistent with each other and are all within 1.5 sigma of Hölzer *et al.*^[9] Optimising the calibrations to minimise the across detector systematic error for the Cr K β profile peak energy leads to a value for the energy to be within one σ of the previous measurement. This shows an ability of this calibration method to be tuned to different energies within the same data set through the minimisation of the systematic error at those energies. Table 3 shows the averages of these various contributions to energy uncertainty for a single Cr K β spectrum as outlined in Section on Determination of Energy Uncertainty.

Definition of chromium K β standard

K β peak energy

All five calibrations based on minimising measures (a)–(e) are consistent. It is reasonable to report any of these results. By definition, the calibration that worked best is based on measure (e), the calibration that minimises the χ_r^2 value of the Cr K β peak energy measurements (Fig. 4(e)). This dispersion function calibration is used in the remainder of the paper.

The weighted mean results in a measurement of the Cr K β profile peak energy of 5946.68(14) eV. This 24 ppm uncertainty is larger than that for an individual fit given in Table 3 and is a result of the remaining systematic error between wedge positions and positions across angle and the detector. Comparing this value to the prior theoretical literature value of 5947.1(10) eV,^[6] the 0.42 eV discrepancy is just over 0.42 standard deviations and is a reflection of the theoretical imprecision. Further, this is an improved result compared with that of the current theory.^[6]

Conversely, the prior experimental literature value of 5946.823(11) eV (1.7 ppm uncertainty)^[4,9] is a more accurate determination of the peak energy for that specific experimental configuration. The discrepancy is 0.143 eV or about 1.01 standard deviations so is in excellent agreement even in this difficult

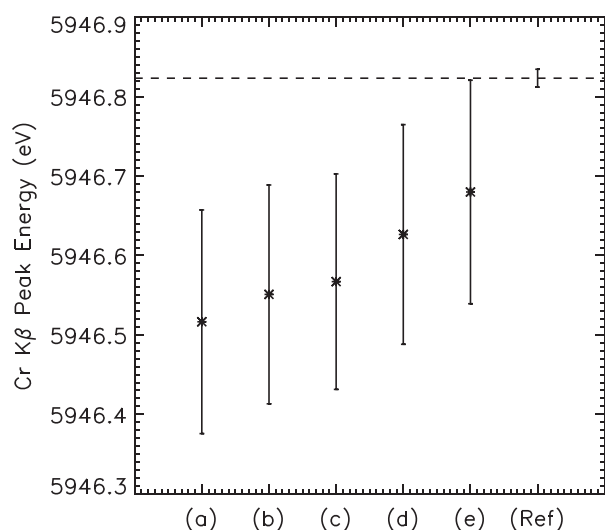


Figure 5. The mean peak energies of the fits of individually measured Cr $K\beta$ spectra for each optimisation method compared to the literature value. Note that all of these, despite different ansatz, yield results consistent with one another to within one standard error. Further, the optimised method focussing on the region of interest gives the highest accuracy and lies within one standard error of the best literature value for the peak energy.^[9]

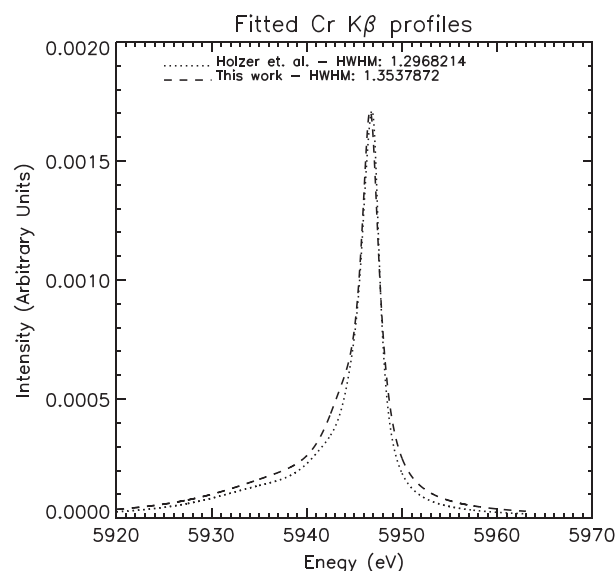


Figure 6. The spectral profile of Cr $K\beta$ measured in this work (dashed line) compared to that reported in Hölzer *et al.*^[9] (dotted line). As presented here, the dashed line is a sum of 3 Lorentzians with parameters given in Table 2. This corresponds to setting the Gaussian width that represents instrumental broadening to 0 eV. The resolution and half width at half maxima (HWHMs) of the two results are in agreement to within 4%. Being a sum of 6 Lorentzians, the characterisation in Hölzer *et al.*^[9] is smoother. This is expected as the 1.4 eV instrumental broadening obtained in the current work smooths out the spectrum so that Hölzer *et al.*^[9] can capture some higher resolution information. It should be noted that Hölzer *et al.*^[9] deconvolved the $K\beta$ spectrum before fitting with an unreported broadening.

Table 3. Typical uncertainty budget for the peak energy of each of the spectral profiles of Cr $K\beta$ in the final plots and which contribute to the energy determination

Uncertainty source	Average contribution to energy uncertainty for an individual Cr $K\beta$ spectrum (ppm)
Cr $K\beta$ spectrum fit ($\frac{\partial E}{\partial x} \Delta x_{fit}$)	1.0
Detector dispersion function fit ($\sqrt{\sum_{ij} \frac{\partial E}{\partial P_{Dj}} \frac{\partial E}{\partial P_{Dj}} C_{D,ij}}$)	0.21
Clinometer noise ($\frac{\partial E}{\partial V} \Delta V$)	1.3
Clinometer calibration fit ($\sqrt{\sum_{ij} \frac{\partial E}{\partial P_{ij}} \frac{\partial E}{\partial P_{ij}} C_{ij}}$)	0.93
Total uncertainty	1.9

The energy measurements show evidence of an unknown variance, likely involved in the experimental and geometrical parametrisation but includes any uncertainty from theory for known and estimated wedge positions. Therefore, the final energy determination has a larger uncertainty than this ideal 1.9 ppm for the individual spectrum, as required and determined by the observed variance. The independent self-consistency shown in this work is invaluable in uncovering sources of systematic uncertainty that might otherwise go unnoticed and remain unanalysed.

arrangement (at the edge of the calibration series). An advantage of the characterisation presented in this work is that the error bars on the characterisation allow for profile and geometry-dependent variation and, more particularly, prove the methodology used here and in prior papers down to a valuable limit. A comparison of the profile fit in Hölzer *et al.*^[9] and this work is presented in Fig. 6.

Conclusion

The spectral profile of Cr $K\beta$ was measured and characterised in a transferable way. The characterisation involved modelling the profile with four Lorentzian peaks convolved with a common Gaussian. The Gaussian is recommended to model additional (instrumental) broadening, so long as significant profile vignetting is not involved, that is, that the profiles are complete $K\beta$ profiles not truncated by the source size or a slit width. This method will reveal the significance of any such vignetting by returning a high χ^2 value for the fits and by being strongly dependent on crystal or diffracting angle. The individual widths and component parametrisation are given explicitly for each component. The Cr $K\beta$ peak energy was found to be 5946.68(14) eV. This is a 24 ppm result. The component modelling is reliable and a recommended standard methodology for future X-ray calibration. Most importantly, this study demonstrates that even near the edge of a calibrated region, with strong variance of results from systematics, the computed final uncertainties accurately reflect the uncertainty of the measurement, even when modelled by a range of distinct optimisations.

Acknowledgements

The authors acknowledge the experimental team, including Mark Kinnane, as well as funding from the ARC for this work. We acknowledge the assistance of our collaborators at the Oxford EBIT including David Crosby.

References

- [1] C. T. Chantler, M. N. Kinnane, J. D. Gillaspay, L. T. Hudson, A. T. Payne, L. F. Smale, A. Henins, J. M. Pomeroy, J. N. Tan, J. A. Kimpton, E. Takacs, K. Makonyi, Testing three-body quantum electrodynamics with trapped Ti^{20+} ions: evidence for a Z-dependent divergence between experiment and calculation, *Phys. Rev. Letts.* **2012**, *109*, 153001–1–5.
- [2] A. T. Payne, C. T. Chantler, M. N. Kinnane, J. D. Gillaspay, L. T. Hudson, L. F. Smale, A. Henins, J. A. Kimpton, E. Takacs, Helium-like titanium X-ray spectrum as a probe of QED computation, *J. Phys.* **2014**, *B47*, 185001–1–8.
- [3] C. T. Chantler, J. A. Lowe, I. P. Grant, Multiconfiguration Dirac–Fock calculations in open-shell atoms: convergence methods and satellite spectra of the copper $K\alpha$ photoemission spectrum, *Phys. Rev. A* **2010**, *82*(5), 052505.
- [4] J. A. Bearden, A. F. Burr, Reevaluation of X-ray atomic energy levels, *Rev. Mod. Phys.* **1967**, *39*(1), 125–142.
- [5] J. P. Desclaux, *At. Data Nucl. Data Tables* **1973**, *12*, 312.
- [6] R. D. Deslattes, E. G. Kessler, P. Indelicato, L. de Billy, E. Lindroth, J. Anton, X-ray transition energies: new approach to a comprehensive evaluation, *Rev. Mod. Phys.* **2003**, *75*(1), 35–99.
- [7] I. P. Grant, *Adv. Phys.* **1970**, *19*, 747.
- [8] M. Deutsch, G. Hölzer, J. Härtwig, J. Wolf, M. Fritsch, E. Förster, $K\alpha$ and $K\beta$ X-ray emission spectra of copper, *Phys. Rev. A* **1995**, *51*(1), 283–296.
- [9] G. Hölzer, M. Fritsch, M. Deutsch, J. Härtwig, E. Förster, $K\alpha_{1,2}$ and $K\beta_{1,3}$ X-ray emission lines of the 3d transition metals, *Phys. Rev. A* **1997**, *56*(6), 4554–4568.
- [10] L. F. Smale, C. T. Chantler, J. A. Kimpton, D. N. Crosby, M. N. Kinnane, Characterization of K beta spectral profile for vanadium, *Phys. Rev.* **2013**, *A87*: 022512–1–7.
- [11] C. T. Chantler, L. F. Smale, J. A. Kimpton, D. N. Crosby, M. N. Kinnane, A. J. Illig, Characterization of titanium K beta spectral profile, *J. Phys.* **2013**, *B46*: 145601–1–10.
- [12] A. J. Illig, C. T. Chantler, A. T. Payne, Voigt profile characterisation of copper K alpha, *J. Phys.* **2013**, *B46*: 235001–1–11.
- [13] C. T. Chantler, A. C. L. Hayward, I. P. Grant, Theoretical determination of characteristic X-ray lines and the copper $K\alpha$ spectrum, *Phys. Rev. Lett.* **2009**, *103*(12), 123002.
- [14] J. A. Lowe, C. T. Chantler, I. P. Grant, A new approach to relativistic multi-configuration quantum mechanics in titanium, *Phys. Lett. A* **2010**, *374*(47), 4756–4760.
- [15] C. T. Chantler, J. A. Lowe, I. P. Grant, Multiconfiguration Dirac–Fock calculations in open-shell atoms: convergence methods and satellite spectra of the copper $K\alpha$ photoemission spectrum, *Phys. Rev. A* **2010**, *82*(5), 052505.
- [16] J. A. Lowe, C. T. Chantler, I. P. Grant, *Phys. Rev. A* **2011**, *83*(6), 060501.
- [17] D. F. Anagnostopoulos, R. Sharon, D. Gotta, D. Moshe, $K\alpha$ and $K\beta$ X-ray emission spectra of metallic scandium, *Phys. Rev. A* **1999**, *60*(3), 2018–2033.
- [18] D. F. Anagnostopoulos, D. Gotta, P. Indelicato, L. M. Simons, Low-energy X-ray standards from hydrogenlike pionic atoms, *Phys. Rev. Lett.* **2003**, *91*(24), 240801.
- [19] J. Schweppe, R. D. Deslattes, T. Mooney, C. J. Powell, Accurate measurement of Mg and Al $K\alpha_{1,2}$ X-ray energy profiles, *J. Electron. Spectrosc. Relat. Phenom.* **1994**, *67*(3), 463–478.
- [20] C. T. Chantler, M. N. Kinnane, C. H. Su, J. A. Kimpton, Characterization of $K\alpha$ spectral profiles for vanadium, component redetermination for scandium, titanium, chromium, and manganese, and development of satellite structure for $z = 21$ to $z = 25$, *Phys. Rev. A* **2006**, *73*(1), 012508.
- [21] S. P. Limandri, A. C. Carreras, R. D. Bonetto, J. C. Trincavelli, $K\beta$ satellite and forbidden transitions in elements with $12 \leq z \leq 30$ induced by electron impact, *Phys. Rev. A* **2010**, *81*, 012504.
- [22] A. S. Koster, H. Mendel, X-ray k emission spectra and energy levels of compounds of 3D-transition metals–I: oxides, *J. Phys. Chem. Solids* **1970**, *31*(11), 2511–2522.
- [23] M. Uršič, M. Kavčič, M. Budnar, Second order radiative contributions in the $K\beta_{1,3}$ X-ray spectra of 3D transition metals and their dependence on the chemical state of the element, *Nucl. Instrum. Methods Phys. Res., Sect. B* **2003**, *211*(1), 7–14.
- [24] S. Morita, J. Fujita, $K\beta$ X-ray transition energies of M-shell-ionized ions of Ti through Ni in a plasma, *Phys. Rev. A* **1985**, *31*(5), 3299.
- [25] L. Mandić, S. Fazinić, M. Jakšić, Chemical effects on the $K\beta_{\{2,5\}}$ and $K\beta_{\{2,5\}}$ X-ray lines of titanium and its compounds, *Phys. Rev. A* **2009**, *80*(4), 042519.
- [26] J. D. Silver, A. J. Varney, H. S. Margolis, P. E. G. Baird, I. P. Grant, P. D. Groves, W. A. Hallett, A. T. Handford, P. J. Hirst, A. R. Holmes, D. J. H. Howie, R. A. Hunt, K. A. Nobbs, M. Roberts, W. Studholme, J. S. Wark, M. T. Williams, M. A. Levine, D. D. Dietrich, W. G. Graham, I. D. Williams, R. O'Neil, S. J. Rose, The Oxford electron-beam ion trap: a device for spectroscopy of highly charged ions, *Rev. Sci. Instrum.* **1994**, *65*(4), 1072–1074.
- [27] M. Deutsch, M. Hart, E. Cummings, *Phys. Rev. B* **1990**, *42*, 1248.
- [28] C. T. Chantler, X-ray diffraction of bent crystals in Bragg geometry. I. Perfect-crystal modelling, *J. Appl. Crystallogr.* **1992**, *25*(6), 674–693.
- [29] C. T. Chantler, X-ray diffraction of bent crystals in Bragg geometry. II. Non-ideally imperfect crystals, modelling and results, *J. Appl. Crystallogr.* **1992**, *25*(6), 694–713.

APPENDIX

We here discuss the calibration of the energy axis. This is the definition form of the dispersion function through calibration functions, the method of propagating error bars through the calibration functions to find uncertainty in energy and a method finding dispersion function through calibration function fitting.

Dispersion function

Two calibration functions are required to map the dispersion function and detector profile to an absolute energy axis. The clinometer calibration function $I(V; P_I)$ maps the clinometer voltage V to the clinometer angle I , while the supplementary relation $\theta = -I$ maps the clinometer angle to the dispersion crystal angle θ which reflects the theoretical Mosplate model crystal angle, thus:

$$\theta = -I(V; P_I) \quad (\text{A.1})$$

$I(V; P_I)$ is defined to be:

$$I(V; P_I) = \arcsin\left(\frac{V - P_{I,2}}{P_{I,0}}\right) - P_{I,1} + \sum_{i=0}^n P_{I,(i+3)}(V - P_{I,2})^i \quad (\text{A.2})$$

where P_I is the vector of fitting parameters.

A second calibration function, the detector dispersion calibration function $D_2(x; P_D)$, maps the recorded detector position x in output units to the theoretical detector position D in mm. The map from x to D was defined by:

$$D_2(x; P_D) = \sum_{i=0}^1 P_{D,i} x^i \quad (\text{A.3})$$

where P_D is the vector of fitting parameters.

Using this calibration, an energy can be assigned for any detector position x and any clinometer voltage V :

$$E(x, V; P_D, P_I) = E_{\text{mos}}(D_2(x; P_D), -I(V; P_I)) \quad (\text{A.4})$$

Eqns A.2 and A.3 define the calibration of an experimental configuration (i.e. wedge position). The calibration process was reduced to simultaneously finding the P_I and P_D fitting parameters that best fit the $K\alpha$ data possibly combined with a minimisation of the variance of another interesting line's measured peak energy at the same time (in this experiment: Ti $K\beta$, V $K\beta$ or Cr $K\beta$). This optimised the statistical information for the determination of the $K\beta$ profile peak energy and the dispersion function.

Determination of energy uncertainty

Following Eqn A.4, the uncertainty in the energy assigned to a detector position measurement, ΔE , was due to four sources of uncertainty:

1. the determination of the detector position (Δx),
2. the detector dispersion fit $C_{D,ij}$,
3. the noise in clinometer voltage (ΔV), and
4. the clinometer calibration function fitting $C_{I,ij}$.

$$\Delta E^2 = \left(\frac{\partial E}{\partial x} \Delta x\right)^2 + \sum_{ij} \frac{\partial E}{\partial P_{D,i}} \frac{\partial E}{\partial P_{D,j}} C_{D,ij} + \left(\frac{\partial E}{\partial V} \Delta V\right)^2 + \sum_{ij} \frac{\partial E}{\partial P_{I,i}} \frac{\partial E}{\partial P_{I,j}} C_{I,ij} \tag{A.5}$$

where $C_{D,ij}$ is the i, j th element of the covariance error matrix from the detector dispersion function fit while $C_{I,ij}$ is the i, j th element of the covariance error matrix from the clinometer calibration function fit.

The clinometer calibration function covariance includes all uncertainties from clinometer nonlinearity, peak and energy uncertainty of $K\alpha$ transitions and fitting, diffraction theory uncertainty and variance and other contributions. While the $K\alpha$ peak position uncertainties are as detailed in Table 1, the uncertainties of the refractive index correction and temperature variation are approximately 1 ppm. Indeed, any temperature uncertainty primarily cancels in the modelling. The impact of uncertainty of the source position upon the diffraction computations is almost negligible. Further, the correlated uncertainty of more complex diffraction estimates cancels to first order.

Calibration function fitting

The specific process which was undertaken to find the fitting parameters P_I and P_D for each calibration followed four major steps: the clinometer pre-calibration; the clinometer calibration first estimate; the calibration fitting; and the detector scale correction. First, preliminary clinometer pre-calibration entailed an experimental characterisation of the angle of incline to voltage function ($V_{pre}(I)$) of the clinometers in isolation:

$$V_{pre}(I) = P_{V,0} \sin(I - P_{V,1}) - P_{V,2} + \sum_{i=0}^8 P_{V,(i+4)} V^i \tag{A.6}$$

Second, an estimate of the clinometer calibration function was constructed by generating data with the $V_{pre}(I)$ function, inverting

the data and then fitting these data with $I(V; P_I)$ (Eqn A.2) where the order of the polynomial was set to $n = 3$.

Third, calibration fitting was a four stage process beginning with estimation of P_I and P_D . Each stage made a refinement of either P_I or P_D through one round of fitting.

The first was to fit the $I(V; P_I)$ function to I_{data} versus V where I_{data} is a set of calculated data predicting the expected clinometer angle for each peak based on the energy and detector position:

$$I_{data} = -\theta_{mos}(D(x, P_D), E) \tag{A.7}$$

It has uncertainty ΔI_{data} :

$$\Delta I_{data}^2 = \left(\frac{\partial \theta_{mos}}{\partial E} \Delta E\right)^2 + \left(\frac{\partial \theta_{mos}}{\partial D}\right)^2 \left(\sum_{ij} \frac{\partial D}{\partial P_{D,i}} \frac{\partial D}{\partial P_{D,j}} C_{D,ij} + \left(\frac{\partial D}{\partial x} \Delta x\right)^2\right) \tag{A.8}$$

This first fit allowed only allows the refinement of $P_{I,1}$ (the overall offset to $I(V; P_I)$).

The second stage was a refit of I_{data} versus V with $I(V; P_I)$ using the P_I from fit 1 as a estimate, this time only allowing the refinement of $P_{I,4}$ through $P_{I,7}$, fitting the fine details and secondary functional parameters of $I(V; P_I)$.

The third stage was to fit $D(x; P_D)$ to D_{data} versus x , where D_{data} is a set of calculated data that provides the expected theoretical detector position for each peak based on the energy and crystal angle:

$$D_{data} = D_{mos}(E, -I(V; P_I)) \tag{A.9}$$

It has uncertainty ΔD_{data} :

$$\Delta D_{data}^2 = \left(\frac{\partial D_{mos}}{\partial E} \Delta E\right)^2 + \left(\frac{\partial D_{mos}}{\partial \theta}\right)^2 \left(\sum_{ij} \frac{\partial I}{\partial P_{I,i}} \frac{\partial I}{\partial P_{I,j}} C_{I,ij} + \left(\frac{\partial I}{\partial V} \Delta V\right)^2\right) \tag{A.10}$$

Both P_D parameters were free in this fit.

Lastly, results from the third stage were then used to refit I_{data} versus V using $I(V; P_I)$, allowing the refinement of $P_{I,4}$ through $P_{I,7}$, as in the second fit. This method generates the P_I and P_D parameters along with associated covariance error matrices C_I from the fourth fit and C_D from the third fit.

At the end of this four stage step, the fitted P_I parameters characterised how the clinometers functioned in the setup through fitting the interlinked $K\alpha$ peak energy, peak position and clinometer voltage calibration data.